Journal of Magnetic Resonance 205 (2010) 196–201

Contents lists available at ScienceDirect

Journal of Magnetic Resonance

journal homepage: www.elsevier.com/locate/jmr

Compressed sensing of remotely detected MRI velocimetry in microfluidics

Jeffrey Paulsen, Vikram S. Bajaj *, Alexander Pines

Department of Chemistry, University of California, Berkeley, CA, United States
Materials Sciences Division, Lawrence Berkeley National Laboratory, Berkeley, CA, United States

ARTICLE INFO

Article history:
Received 7 January 2010
Revised 16 April 2010
Available online 8 June 2010

Keywords:
Microfluidics
Remote detection
Velocimetry
Flow imaging

ABSTRACT

NMR and MRI can yield detailed chemical and dynamic information about flow at microscopic resolutions, but suffer from low signal to noise relative to alternative techniques for flow measurements. In porous media and microfluidic devices, this sensitivity problem is further exacerbated by magnetic susceptibility broadening and low coil filling factor. Fortunately, remote detection can mitigate these issues by physically separating signal detection from the other steps of the experiment. The technique requires, however, that any measured interactions be encoded in indirectly sampled dimensions, leading to experiments of high dimensionality and correspondingly long acquisition times. We have applied compressed sensing, a reconstruction technique used in MRI, to dramatically reduce these experiment times by 8–64× through partial sampling (sub-sampling) of k-space, allowing for the collection of images with significantly higher resolutions in reasonable amounts of time. Here, we demonstrate this reconstruction technique to remotely detected flow measurements in a serpentine mixing chip and in a microfluidic channel harboring a constriction. We find that compressed sensing allows for significantly higher resolution images to be collected in a practical amount of time, thus significantly enhancing the applicability of remote detection to flow imaging.

1. Introduction

Of the many techniques available to study flow in small devices, the most commonly applied are based on optical particle tracking and ultrasound. NMR and MRI, however, are unique in their ability to provide both chemical and dynamic information about the flow field in three spatial dimensions. Indeed, MRI measurements can yield the complete flow propagator in favorable cases, at microscopic resolution and even in opaque materials. For example, MRI has been used to study complex fluid dynamics and rheological properties [1,2], flow and mixing in microfluidic channels [3], fluid flow in porous media [4–6], and to study oil and water in situ in oil well logging applications [7]. In all these cases, MRI can be applied in unperturbed native systems, obviating the need for artificial model systems with carefully tailored optical properties.

One important potential domain of application for MRI velocimetry is microfluidics, in which control over fluid dynamics on microscopic length scales is exploited to create 'lab on a chip' devices that can parallelize and miniaturize complex laboratory tasks. These tasks include the optimization of crystal growth conditions [8], supporting and monitoring live cell cultures [9,10], and complex chemical analyses [11–14]. To those ends, a variety of microfluidic components have been developed, including microchromatography columns [15,16], pumps [17–20], valves [20–22], MEMS [23,24], and micro-optofluidic devices [13,25,26]. However, the design and optimization of these devices is hindered by the lack of techniques that can fully characterize flow and dispersion within them.

While MRI is one such technique, its low sensitivity remains a major challenge, one that is exacerbated by the low filling factors and the significant magnetic susceptibility broadenings typical of porous and microfluidic systems. Fortunately, many of these factors can be mitigated by remote detection, a method which encodes and stores the spatial and chemical information into the spin degrees of freedom of the flowing fluid and detects it as the fluid reaches an optimized detector [27,28]. In remote detection, encoding occurs over the entire volume of the structure (e.g. cm-scale microfluidic chip, bead pack, rock sample), while the detector volume is matched to the volume of fluid in the features to be imaged (μm scale). The encoding step may include delays for chemical shift evolution and relaxation, and gradient pulses for multiple spatial dimensions, velocity encoding and even measurements of acceleration, or higher order moments of the motion. The sensitivity enhancements possible with remote detection [29] can be several orders of magnitude for microfluidic and microporous structures. However, all encoded interactions must be sampled in indirect dimensions, and their exhaustive Fourier sampling potentially leads to prohibitively long acquisition times.

* Corresponding author.
E-mail addresses: vikbajaj@gmail.com, vsbajaj@lbl.gov (V.S. Bajaj).

1090-7807/$ - see front matter © 2010 Elsevier Inc. All rights reserved.
doi:10.1016/j.jmr.2010.04.016

In this work, we dramatically reduce the required acquisition times (8–64×) for remotely detected MRI experiments by the application of compressed sensing, a method that has been used to accelerate image acquisitions in clinical MRI [30,31] where it shows great promise in applications requiring accelerated acquisition, including hyperpolarized spectroscopic imaging [32] and cardiac imaging [33]. Compressed sensing is a general non-linear reconstruction technique that can be applied to subsampled data in many contexts beyond NMR and Fourier reconstruction [34,35]. The technique relies on the notion of transform sparsity, in which most of the signal of an image under the appropriate transformation is concentrated into a small fraction of the coefficients that span the transform space, and a reconstruction that will encourage a sparse fit to the acquired data. In its application, we reconstruct an image from observed data by performing an l_1-norm optimization on such a sparse representation of the reconstruction. The vast majority of images have transform sparsity, and this is exploited in many image compression formats, for instance JPEG2000. Furthermore, others have shown that non-linear reconstruction techniques like maximum entropy and l_1-norm minimization perform far better when the reconstructed data set is sparse [36]. Compressed sensing is a formalized generalization of this idea, as the optimization is performed on a sparse representation of the reconstruction [30,32].

The results of an exhaustively sampled imaging experiment can be uniquely inverted by the Fourier transform to yield a single image; an undersampled data set, however, is consistent with a family of images. Therefore, the goal of our reconstruction algorithm, outlined in Fig. 1A, is to search for an image that is consistent with the experimental data but also sparse. Mathematically, this is done by minimizing the l_1-norm of a sparse representation of the image (the sum of the individual pixel magnitudes), while also enforcing consistency of that image with the data that were actually collected. In the examples we present, we reconstruct MRI images by minimizing the l_1-norm of the *wavelet representation* of the trial image while simultaneously enforcing consistency of that image, when transformed back into the conjugate k-space, with the experimentally measured data. The algorithm stops when convergence criteria are met indicating that the l_1-norm has been minimized for the given tolerance to the acquired data. Minimizing the l_1-norm is a well-known method to find sparse reconstructions of otherwise inadequately sampled data, and is, indeed, one of several methods to find sparse representations of data, often referred to as basis pursuit.

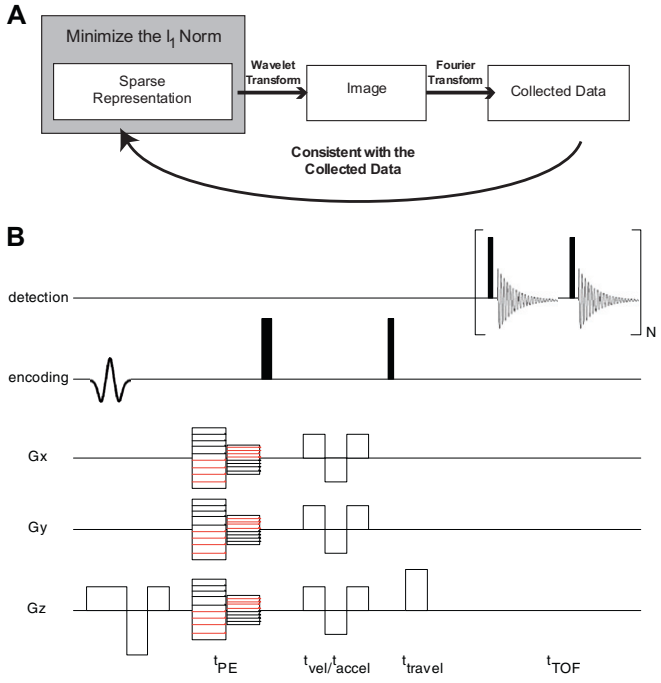

Fig. 1. (A) Data reconstruction with compressed sensing. The technique minimizes the l_1-norm of the sparse representation of the image that is consistent with the collected data. Linear transforms relate the sparse domain to the reconstruction (i.e. wavelet) and the reconstruction to the collected data i.e. Fourier transform. (B) The pulse sequence for a remotely detected MRI experiment with velocity encoding. The experiment starts with slice selective excitation in one dimension, followed be phase encoding (t_{PE}) and velocity encoding (t_{vel}) within a spin echo sequence. The total encoding times are less than 1 ms in all cases. The experiment ends by storage of the encoded information as longitudinal magnetization, followed by travel to the optimized microcoil detector, where the encoded information is read stroboscopically.

Stating the reconstruction algorithm exactly, given the collected data *in k-space*, k_i, and a series of linear transforms to relate the sparse representation of the reconstruction to the collected data $\bar{R}$, and $\bar{S}$, whose inverses respectively reconstruct the fully sampled data and generate a sparse representation of the reconstruction, the appropriate optimization is [30,37]:

$$\min |s_i|^1 \text{st}$$
$$\|\bar{R}\bar{S}s_i - k_i\|^2 \leqslant \varepsilon^2$$

The variable ε controls the strength of the constraint and is set to be large enough to guarantee convergence of the optimization in a reasonable amount of time, while still enforcing agreement with the collected data. Performing an optimization with an 'exact' match ($\varepsilon = 0$) takes several times longer to produce insignificant changes to the reconstruction. Alternatively, ε can be set to a significant fraction of the image's overall noise level to yield a reduction in the appearance of noise due to the additional regularization this allows. The algorithm is straightforward to implement and requires only the selection of optimization parameters and methods, and the choice of transform to yield a sparse representation. For example, this might involve one of several freely available packages capable of large scale l_1 optimizations, and an implementation of the fast wavelet transform [38] to yield a sparse representation of the reconstruction. The choice of the most appropriate transform depends on the reconstructed data: for images of objects with generic structure like the brain [37], wavelet transforms are commonly employed, but for angiograms [33,37] or images of objects with sharp edge features, a finite-difference transform may be more appropriate.

MRI images of microfluidic devices are comparatively sparse, characterized by small-scale features over large length scales. This makes the application of compressed sensing particularly appealing because transform sparsity is easily obtained and, in general, the data will not satisfy the more stringent requirements (e.g. specific functional forms such as an oscillating exponential decay) of many sub-sampling techniques commonly applied in NMR spectroscopy [39]. Furthermore, the multiple dimensions required in remotely detected MRI velocimetry experiments provide tremendous flexibility in the implementation of a sub-sampling schedule. Here we have used sparse encoding in the wavelet basis to implement compressed sensing for the MRI analysis of a microfluidic mixer and a microfluidic chip harboring a constriction, achieving reductions in acquisition times between 8 and 64×.

2. Methods

All experiments with the mixing chip were performed on a 300 MHz Oxford Instruments wide bore magnet with a Varian console and 30 mm imaging system capable of producing 100 G/cm magnetic fields on all axes. Experiments with the microfluidic weir chip were acquired on a similar 300 MHz Varian system with a

three-axis gradient set capable of generating 60 G/cm gradients along the *Z*-axis and 80 G/cm on the *X*- and *Y*-axes. The remote detection probe setup and pulse sequence is briefly summarized here and detailed elsewhere. The apparatus consists of a custom built microcoil probe with a single capillary connecting the microcoil circuit to the microfluidic chip held in a plastic holder. The microcoil probe is inserted above a standard 30 mm proton imaging probe, used for encoding, such that the mircofluidic chip is centered in the 30 mm imaging probe's sensitive region. A steady flow of distilled and filtered water is maintained through the system by pressurizing a supply tank with N_2 gas at constant pressure (0–100 psi). Bubbling within the lines is prevented by the addition of a small amount of isopropanol (1–2 vol.%) to the water.

The pulse sequence for remote detection (Fig. 1B) involves spatial and velocity encoding by multi-lobe gradients within a spin echo imaging sequence. The shapes of these gradient pulses are chosen for velocity or acceleration compensated spatial and velocity encoding as detailed in [40]. The phase encoded signal is stored longitudinally and detected after flow to the microcoil detector using a stroboscopic sequence, yielding both the NMR spectra and the time-of-flight. The excitation pulse, storage pulse, and receiver phases are cycled in a four step phase cycle to achieve hypercomplex detection, subtraction of signals from unencoded spins, and artifact suppression.

3. Data reconstruction

The reconstruction code was programmed in Matlab using two external packages, spgl1 v.1.7 [41] and Wavelab v.8.02 [42]. Spgl1 is a general l_1-norm optimizer that can operate upon complex numbers, parametrically call external objective functions that relate the sparse domain and the collected data, and allows for an inequality constraint to the collected data as is necessary for noise reduction. Sparsifying transforms were implemented with Wavelab, a package written for Matlab capable of calculating the fast wavelet transform for a variety of wavelets. Prior to reconstruction of the subsampled image, the direct dimension is apodized and processed using a conventional Fourier transformation, and the intensity corresponding to each spectral line extracted by complex integration (in the case of water, there is one spectral line). Reconstructions of subsampled data are performed using the l_1-norm optimization problem stated in the introduction, and with the above software libraries. We apply these separately to generate a pair of complex valued images for each of the values of the velocity encoding gradient. Further, the calculation is performed separately for each time-of-flight image, taking 2–10 min per 256×256 velocity encoded image. The noise parameter (or looseness of the fit), ε^2, is set to approximately one-tenth the value of the noise level calculated from the early time-of-flight points, corresponding to experimental time points that precede the arrival of encoded fluid at the detector. The velocity is then calculated as the phase difference between the two reconstructed complex valued images for the two values of the velocity encoding gradient (positive and negative), separately for each time-of-flight. For a time-of-flight averaged view of an experiment, reconstructions from times-of-flight with significant signal are added together. To simultaneously visualize the velocity and image intensity, the velocity encoded data is plotted so that the hue (color) is scaled according to the velocity and the saturation according to the signal intensity.

4. Sampling optimization

The choice of the sampling schedule has a strong influence on the quality of reconstructions possible with the technique, as shown in Fig. 2, because the sampled points must contain non-redundant information about all of the sparse coefficients as described in [37] while simultaneously sampling regions of the transform space where the signal is concentrated. The purpose of our optimization was to avoid such possible pathological sampling schemes, and find ones with generally good performance that could be applied without specific consideration of the geometry. Thus, we do not necessarily find the most optimized sampling for a specific geometry. The optimization of sampling for compressed sensing is entirely analogous to the problem of choosing the appropriate sub-sampling schedule for other NMR reconstruction techniques [37], except that the sparse transform of the reconstruction instead of the reconstruction itself is relevant, and one has the additional freedom of selecting this transform.

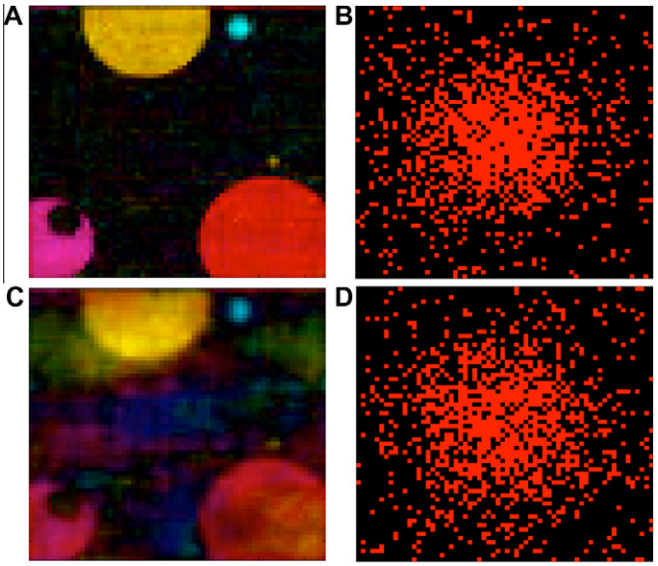

Fig. 2. The reconstruction of an artificial dataset with two different sampling schemes. The sampling tables are for 4× subsampled 64×64 images and represent the best and worst sampling schemes generated by repeatedly creating samplings from the same Gaussian distribution. Even with the same distribution, a large variation in reconstruction performance is apparent between the two reconstructions (A and C) despite the similar appearance of the corresponding sampling schemes plotted right (B and D). Here, the plots indicate each reconstruction's intensity as value (black to full intensity) and phase as hue (color).

For use as a sparsifying transform, we selected wavelet transforms due to their known applicability to a wide variety of images (indeed, they are used in JPEG2000 image compression) and the availability of several well-developed implementations. In particular, we selected the symmlet wavelet because, in the case of very low SNR or inappropriate sampling schedules, it produced only a mild blurring artifact, while other wavelet types produced generally harsher spikes and discontinuities. Finally, we note that, while sparsification based on finite difference representation may be appropriate for analogous applications in angiography, it does not seem appropriate in our studies of microfluidic velocimetry. This is because applications in angiography require only determining the extent or edge of a blood vessel, while our measurements seek to elucidate the internal texture of a continuously varying flow field. Indeed, explicit calculations of the sparsity of each approach (see Supporting information) agrees with this intuition: finite difference methods did not perform as well and were not used here.

Having decided on a sparsifying transform, we next chose sampling schedules by optimizing random, Gaussian weighted sampling tables. The weighting was designed to bias the sampling towards the center of k-space. We manually compared these

candidate sampling schedules according to the magnitude of wavelets of different scales that result after passage through transform point spread function (TPSF), giving a heavier weighting to the retention of coarser wavelets. The TPSF indicates how well a particular sampling scheme contains the information required to reconstruct intensities for different wavelet scales, and good retention requires incoherence between the sampling (k-space) and wavelet domains. Further, our emphasis on the coarser wavelets is essential since most of the image's intensity in the wavelet domain is contained here, and poor retention of this information will thus result in significant artifacts. Indeed, Fig. 2 illustrates the dramatic difference between sampling schedules that appear equivalent in the conjugate (k) space, but which differ dramatically in the degree to which they retain coarse wavelet information and which therefore result in significantly different reconstruction quality.

Specifically, to generate a sampling scheme, for each grid size and degree of sub-sampling, we first selected an optimal Gaussian distribution based on the TPSF retentions. The width of this distribution controls the compromise between retention of different wavelet scales. In general, a narrower distribution – one that retains information at coarser wavelet scales at the expense of finer wavelets – became necessary for a satisfactory reconstruction at higher sub-sampling ratios. Finally, the best sampling is selected manually from numerous random trial application of that optimal distribution, based again on the TPSF retentions.

5. Results

In the serpentine microfluidic mixer, we tested four sampling schemes each optimized for 8×, 16×, 32×, and 64× sub-sampling of a 256 × 256 pixel velocity encoded image. A fully sampled 63 × 63 image with the same field of view was collected as a comparison to the 16× subsampled image. A fully sampled 256 × 256 image was not collected due to the prohibitively long acquisition time (~7 days). All experiments produce velocity-encoded images for multiple times-of-flight obtained from different points in the stroboscopic acquisition as shown in Fig. 3. In general, components visible in earlier images are nearest the outlet and reach the detector first, followed by components progressively closer to the inlet. For this reconstruction, we can clearly resolve the flow, chip geometry and flow velocity for each time-of-flight.

Several features of the reconstruction become apparent as we increase the degree of sub-sampling. First, the reconstruction quality gradually declines, as shown in the comparison of time-of-flight averaged images collected at different degrees of sub-sampling in Fig. 4. The threshold at which the reconstruction begins to fail will generally vary depending on the sparsity of the reconstructed image and the experimental signal to noise ratio [30,37]. The velocity-encoded images agree qualitatively up to sub-sampling factors of 16×, while very little degradation is apparent for intensity images up to 32× sub-sampling. It is not surprising that the intensity reproduction is more robust, as the phase contrast technique used in the velocity imaging is significantly more susceptible to noise and artifacts. At 64× sub-sampling, the reconstructed image contains artifacts resembling those from excessive lossy image compression. The form of these artifacts is difficult to predict but reflects the properties of the underlying sparsifying transformation and sampling scheme. However, even such high degrees of sub-sampling may be useful for qualitative binary analyses of presence or absence of an analyte, a common function of analytical microfluidic chips. We also

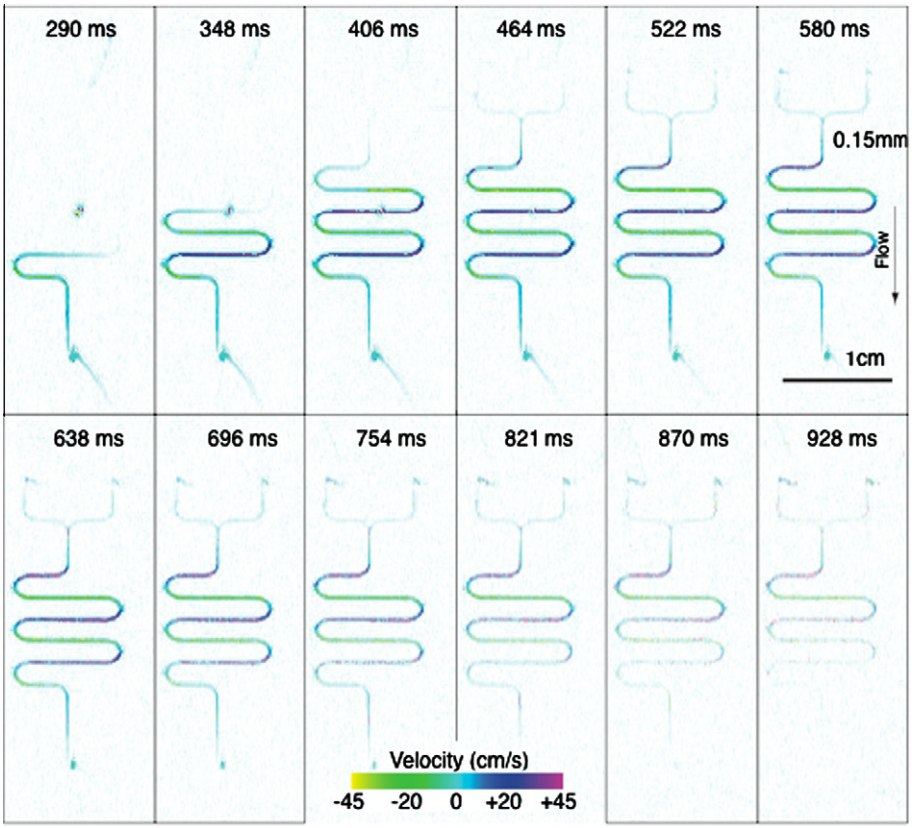

Fig. 3. Images of flow through a serpentine mixing chip acquired with 8× sub-sampling, arranged by time-of-flight. Only the horizontal component of the velocity is encoded and displayed, and hence the sign of the velocity changes as the direction of flow changes relative to the horizontal axis. The time-of-flight corresponds to the period between the encoding and detection. Therefore components nearest the outlet are visible first, while components further back are visible at later times-of-flight.

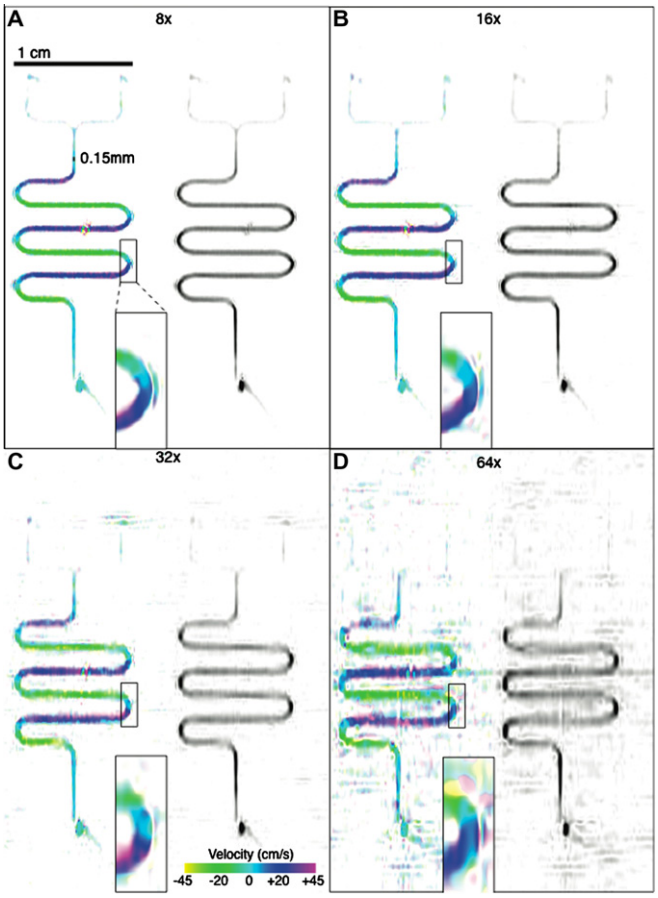

Fig. 4. A comparison of velocity-encoded images of the mixing chip under varying degrees of sub-sampling, summed over multiple times-of-flight, and shown for both velocity and intensity reconstructions. The intensity reconstruction is the sum of the magnitudes of the images generated for each step of the velocity encoding gradient and reflects the relation weighted density of spins in a given voxel. Good qualitative evaluation of the velocity is possible at up to 16× sub-sampling whereas the intensity reconstruction maintains a similar quality with greater sub-sampling, 32×. The artifacts under high degrees of sub-sampling (64×) do not correspond to simple blurring, but instead appear similar to image compression artifacts.

note that in the case of microfluidic devices, the chip geometry is known a priori, and the design of an optimal sampling scheduling using that information may result in higher sub-sampling ratios. Such approaches were not attempted here but work in this direction is presently in progress.

As shown in Fig. 5, sub-sampling can alternatively be used to increase resolution instead of reducing the acquisition time. Both images in the figure were collected with a similar number of points, but the subsampled image clearly yields better resolution and a more accurate representation of the chip than its fully sampled counterpart, and even has the same signal to noise. Here, time equivalent Cartesian sampling is unable to accurately reproduce the channel widths and features of the flow field. Thus, we can arrive at an optimal use of experiment time by finding a compromise between the degree of sub-sampling and resolution.

Since the mixing chip is sparse by inspection and contains rectangular features, it does not represent the broader variety of porous materials for which remote detection might be essential. In order to test the applicability of this technique to irregular systems, we applied compressed sensing to the velocimetry of a microfluidic channel harboring an irregular constriction. The 8× subsampled (64 × 16 × 16) image of this constriction is shown in Fig. 6, and illustrates that compressed sensing is broadly applicable

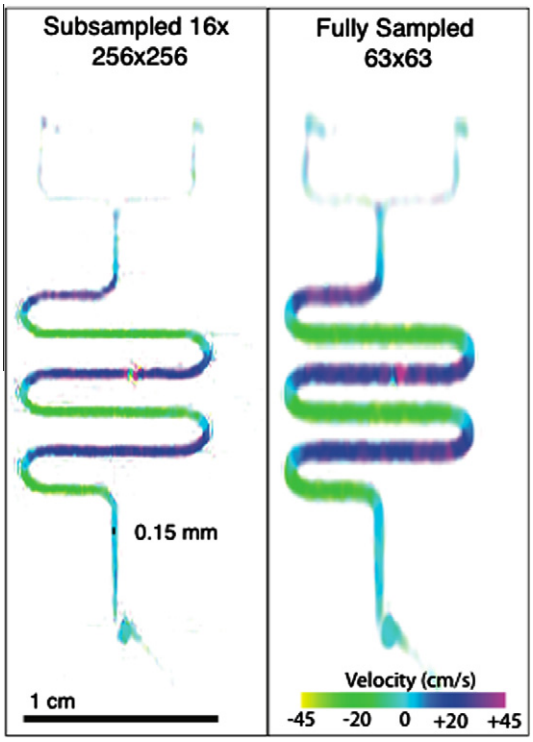

Fig. 5. A direct comparison of a subsampled vs. a fully sampled reconstruction of the mixing chip using a similar number of data points. (Left) A 16× subsampled 256 × 256 image reconstructed with compressed sensing. (Right) The same image fully sampled for 63 × 63 points. Both images are zero-filled by a factor of four and apodized as discussed in the text. The subsampled acquisition accurately reproduces the chip's features (such as channel width) over a field of view that includes the entire chip, whereas these features appear distorted in a fully sampled acquisition collected with a similar number of points.

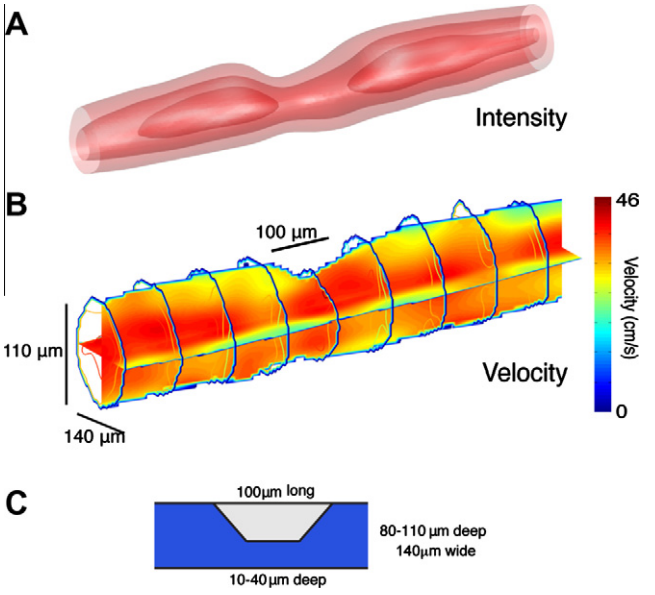

Fig. 6. Flow through a microfludic constriction (or weir) obtained as a velocity encoded 64 × 16 × 16 three-dimensional image subsampled 8×. (a) Spin density image of the constriction. (b) Velocity and spin density image displayed as two intersecting planes that intersect on an axis that is the approximate channel center. The planes are colored according to the velocity. A wireframe contour surrounds the channel and also reflects velocity. Both the constriction and correlated increase in velocity are clearly visible. The subsampled reconstruction accurately reproduces the feature which lacks the immediately apparent sparsity and simple structure of the mixing chip. The application of compressed sensing here lets us examine the feature at higher resolution (~20 µm) with a shorter experiment time than otherwise possible.

to many systems that do not share the sparse features of most microfluidic chips.

6. Conclusions

The successful application of compressed sensing in microfluidic mixers and channels demonstrates that it is a robust technique for remotely detected MRI of microscale flow. Indeed, compressed sensing is particularly attractive because it rests on a strong and formal theoretical basis [30,32] that establishes the conditions under which it will give accurate results. We anticipate that the technique will be widely used in remotely detected NMR because it greatly reduces the experiment times for these high dimensional experiments to more reasonable lengths, expanding its applicability to microfluidics, porous systems, and to analogous *in vivo* flow structures.

Acknowledgments

The authors acknowledge Professor David Wemmer for his careful reading of the manuscript. This work was supported by the Director, Office of Science, Office of Basic Energy Sciences, and Materials Sciences Divisions of the US Department of Energy under contract DE-AC03-76SF0098. We thank Schlumberger-Doll Research and the Agilent Foundation for their unrestricted funds in support of this research.

Appendix A. Supplementary material

Supplementary data associated with this article can be found, in the online version, at doi:10.1016/j.jmr.2010.04.016.

References

[1] R.W. Mair, P.T. Callaghan, Shear flow of wormlike micelles in pipe and cylindrical Couette geometries as studied by nuclear magnetic resonance microscopy, J. Rheol. 41 (1997) 901–924.
[2] P.T. Callaghan, Principles of Nuclear Magnetic Resonance Microscopy, Clarendon Press, Oxford, 1991.
[3] E. Harel, A. Pines, Spectrally resolved flow imaging of fluids inside a microfluidic chip with ultrahigh time resolution, J. Magn. Reson. 193 (2008) 199–206.
[4] L. Li, Q. Chen, A.E. Marble, L. Romero-Zerón, B. Newling, B.J. Balcom, Flow imaging of fluids in porous media by magnetization prepared centric-scan SPRITE, J. Magn. Reson. 197 (2009) 1–8.
[5] Y.E. Kutsovsky, L.E. Scriven, H.T. Davis, B.E. Hammer, NMR imaging of velocity profiles and velocity distributions in bead packs, Phys. Fluids 8 (1996) 863–871.
[6] S. Harms, S. Stapf, B. Blümich, Application of k- and q-space encoding NMR techniques on granular media in a 3D model fluidized bed reactor, J. Magn. Reson. 178 (2006) 308–317.
[7] D.P. Murphy, Advances in MWD and formation evaluation for 1995, World Oil 216 (3) (1995) 39–49 (Other Information: PBD: Mar 1995 Medium: X; Size).
[8] C.L. Hansen, E. Skordalakes, J.M. Berger, S.R. Quake, A robust and scalable microfluidic metering method that allows protein crystal growth by free interface diffusion, Proc. Natl. Acad. Sci. U. S. A. 99 (2002) 16531–16536.
[9] A.R. Wheeler, W.R. Throndset, R.J. Whelan, A.M. Leach, R.N. Zare, Y.H. Liao, K. Farrell, I.D. Manger, A. Daridon, Microfluidic device for single-cell analysis, Anal. Chem. 75 (2003) 3581–3586.
[10] H. Andersson, A. van den Berg, Microfluidic devices for cellomics: a review, Sens. Actuators, B 92 (2003) 315–325.
[11] S.A. Greenspoon, S.H.I. Yeung, K.R. Johnson, W.K. Chu, H.N. Rhee, A.B. McGuckian, C.A. Crouse, T.N. Chiesl, A.E. Barron, J.R. Scherer, J.D. Ban, R.A. Mathies, A forensic laboratory tests the Berkeley microfabricated capillary array electrophoresis device, J. Forensic Sci. 53 (2008) 828–837.
[12] E.T. Lagally, P.C. Simpson, R.A. Mathies, Monolithic integrated microfluidic DNA amplification and capillary electrophoresis analysis system, Sens. Actuators, B 63 (2000) 138–146.
[13] G.M. Whitesides, The origins and the future of microfluidics, Nature 442 (2006) 368–373.
[14] Elisabeth Verpoorte, Microfluidic chips for clinical and forensic analysis, Electrophoresis 23 (2002) 677–712.
[15] D.S. Peterson, Solid supports for micro analytical systems, Lab Chip 5 (2005) 132–139.
[16] N. Tanaka, H. Nagayama, H. Kobayashi, T. Ikegami, K. Hosoya, N. Ishizuka, H. Minakuchi, K. Nakanishi, K. Cabrera, D. Lubda, Monolithic silica columns for HPLC, micro-HPLC, and CEC, J. High Resolut. Chromatogr. 23 (2000) 111–116.
[17] D.J. Laser, J.G. Santiago, A review of micropumps, J. Micromech. Microeng. 14 (2004) R35–R64.
[18] I.M. Lazar, B.L. Karger, Multiple open-channel electroosmotic pumping system for microfluidic sample handling, Anal. Chem. 74 (2002) 6259–6268.
[19] H. Andersson, W. van der Wijngaart, P. Nilsson, P. Enoksson, G. Stemme, A valve-less diffuser micropump for microfluidic analytical systems, Sens. Actuators, B 72 (2001) 259–265.
[20] W.H. Grover, A.M. Skelley, C.N. Liu, E.T. Lagally, R.A. Mathies, Monolithic membrane valves and diaphragm pumps for practical large-scale integration into glass microfluidic devices, Sens. Actuators, B 89 (2003) 315–323.
[21] K.W. Oh, C.H. Ahn, A review of microvalves, J. Micromech. Microeng. 16 (2006) R13–R39.
[22] C. Yu, S. Mutlu, P. Selvaganapathy, C.H. Mastrangelo, F. Svec, J.M.J. Frechet, Flow control valves for analytical microfluidic chips without mechanical parts based on thermally responsive monolithic polymers, Anal. Chem. 75 (2003) 1958–1961.
[23] N.-T. Nguyen, X. Huang, T.K. Chuan, MEMS-micropumps: a review, J. Fluids Eng. 124 (2002) 384–392.
[24] E. Verpoorte, N.F. De Rooij, Microfluidics meets MEMS, Proc. IEEE 91 (2003) 930–953.
[25] D. Psaltis, S.R. Quake, C. Yang, Developing optofluidic technology through the fusion of microfluidics and optics, Nature 442 (2006) 381–386.
[26] C. Monat, P. Domachuk, B.J. Eggleton, Integrated optofluidics: a new river of light, Nat. Photon. 1 (2007) 106–114.
[27] J.A. Seeley, S.-I. Han, A. Pines, Remotely detected high-field MRI of porous samples, J. Magn. Reson. 167 (2004) 282–290.
[28] C. Hilty, E.E. McDonnell, J. Granwehr, K.L. Pierce, S.-I. Han, A. Pines, Microfluidic gas-flow profiling using remote-detection NMR, Proc. Natl. Acad. Sci. U. S. A. 102 (2005) 14960–14963.
[29] J. Granwehr, J.A. Seeley, Sensitivity quantification of remote detection NMR and MRI, J. Magn. Reson. 179 (2006) 280–289.
[30] D.L. Donoho, Compressed sensing, IEEE Trans. Inf. Theory 52 (2006) 1289–1306.
[31] Michael Lustig, David Donoho, John M. Pauly, M.R.I. Sparse, The application of compressed sensing for rapid MR imaging, Magn. Reson. Med. 58 (2007) 1182–1195.
[32] E.J. Candes, J. Romberg, T. Tao, Robust uncertainty principles: exact signal reconstruction from highly incomplete frequency information, IEEE Trans. Inf. Theory 52 (2006) 489–509.
[33] M. Lustig, J.M. Santos, D.L. Donoho, J.M. Pauly, k-t SPARSE: high frame rate dynamic MRI exploiting spatio-temporal sparsity, ISMRM (2006).
[34] D. Takhar, J.N. Laska, M.B. Wakin, M.F. Duarte, D. Baron, S. Sarvotham, K.F. Kelly, R.G. Baraniuk, A new compressive imaging camera architecture using optical-domain compression, in: Proceedings of IS&T/SPIE Computational Imaging IV, 2006.
[35] Y. Tsaig, D.L. Donoho, Extensions of compressed sensing, Signal Process. 86 (2006) 549–571.
[36] D.L. Donoho, I.M. Johnstone, J.C. Hoch, A.S. Stern, Maximum entropy and the nearly black object, J. R. Stat. Soc. B (Methodological) 54 (1992) 41–81.
[37] M. Lustig, D.L. Donoho, J.M. Santos, J.M. Pauly, Compressed sensing MRI, IEEE Signal Process. Mag. 25 (2008) 72–82.
[38] O. Rioul, M. Vetterli, Wavelets and signal processing, IEEE Signal Process. Mag. 8 (1991) 14–38.
[39] M. Mobli, A.S. Stern, J.C. Hoch, Spectral reconstruction methods in fast NMR: reduced dimensionality, random sampling and maximum entropy, J. Magn. Reson. 182 (2006) 96–105.
[40] E. Fukushima, Nuclear magnetic resonance as a tool to study flow, Annu. Rev. Fluid Mech. 31 (1999) 95–123.
[41] E. van den Berg, M.P. Friedlander, Probing the Pareto frontier for basis pursuit solutions, SIAM J. Sci. Comput. 31 (2008) 890–912.
[42] J. Buckheit, S. Chen, D. Donoho, I.M. Johnstone, J. Scargle, About Wavelab, Stanford University Tech. Report, 1995.